Z-mode maser instability

Sibaek Yi,[1] Sang-Yun Lee,[1] Hee-Eun Kim,[1] Dayeh Lim,[1] Jungjoon Seough,[1]
P. H. Yoon,[1,2] M. C. Broughton,[3] and J. LaBelle[3]

[1]   Although the cyclotron maser instability customarily involves the extraordinary (*X*) and ordinary (*O*) fast transverse electromagnetic wave modes, which directly escape and propagate long distances from the source region, the instability also excites the *Z* mode for a wide range of parameters. Even though *Z* mode is a nonescaping mode, it may convert to *O* mode in an inhomogeneous medium and be detected by remote means. This process is believed to explain radio emissions near cyclotron harmonics emitted both upward and downward from Earth's auroral ionosphere, as well as analogous emissions detected near Saturn. A more general analysis of the electron loss cone driven *Z*-mode maser instability than previously reported reveals that for certain plasma-to-cyclotron-frequency ratios, the unstable waves split into broadband and narrowband ranges of unstable modes and that these two bands are characterized by distinct polarizations. In previous studies of the *Z*-mode maser, the maximum growth rate was considered without distinguishing the two bands. Although the maximum temporal growth rate sometimes corresponds to the narrowband feature, the broadband feature with a significant *O*-mode-like polarization may be of importance, since it can more easily convert to an escaping radiation. This paper presents analysis of maximum growth rates, wave propagation angles, and wave frequencies for the two band features of the loss cone driven *Z*-mode maser instability as a function of the ratio of plasma-to-electron cyclotron frequency. The results are relevant to auroral radio emission phenomena, especially those observed near cyclotron harmonics at both Earth and Saturn.

1. Introduction

[2] The classic electron-cyclotron maser instability has a wide range of applicability in space and astrophysical context (for a recent review on this subject, see *Treumann* [2006]). It was first applied to the Earth's auroral kilometric radiation [*Wu and Lee*, 1979; *Lee and Wu*, 1980; *Hewitt et al.*, 1982; *Melrose et al.*, 1984; *Pritchett*, 1984, 1985, 1986; *Winglee and Pritchett*, 1986; *Pritchett and Winglee*, 1989; *Pritchett et al.*, 1999], but the maser mechanism also has a wider range of applicability including the planetary radio emissions [*Zarka*, 1998; *Gurnett et al.*, 2004; *Hess et al.*, 2007; *Menietti et al.*, 2010], solar radio bursts [*Tang and Wu*, 2009; *Wu et al.*, 2012; *Zhao and Wu*, 2013; *Zhao et al.*, 2013], radio emissions from extrasolar planets

[*Farrell et al.*, 1999], radiation at the astrophysical shock fronts [*Bingham et al.*, 2003], and for radio emissions from various stellar environments [*Willes and Wu*, 2004; *Begelman et al.*, 2005; *Hallinan et al.*, 2007, 2008; *Trigilio et al.*, 2011; *Nichols et al.*, 2012]. Recently, laboratory plasma experiments have also addressed this phenomenon [e.g., *Speirs et al.*, 2011].

[3] The customary definition for maser instability involves the escaping radiations in magnetized plasmas, namely, the extraordinary (*X*) and ordinary (*O*) modes. In certain conditions, the maser instability may generate *Z*-mode waves. The *Z* mode is a trapped electromagnetic plasma wave mode. The upper bound of the emission frequency is the angular electron plasma frequency, $\omega_p = \left(\dfrac{4\pi n e^2}{m}\right)^{1/2}$, for parallel propagation and the upper hybrid frequency, $\omega_{uh} = \sqrt{\omega_p^2 + \Omega^2}$, for perpendicular propagation, where $\Omega = eB/mc$ is the electron cyclotron frequency. The lower bound is the *Z*-mode cutoff, $\omega_Z = \dfrac{1}{2}\left(\Omega^2 + \sqrt{\dfrac{\Omega^2}{4} + \omega_p^2}\right)$. In the preceding equations $e, m, c, n,$ and B are the unit electron charge, the electron rest mass, the speed of light in vacuo, the electron number density, and the

[1]School of Space Research, Kyung Hee University, Yongin-Si, Korea.
[2]Institute for Physical Science and Technology, University of Maryland, College Park, Maryland, USA.
[3]Department of Physics and Astronomy, Dartmouth College, Hanover, New Hampshire, USA.

Corresponding author: P. H. Yoon, Institute for Physical Science and Technology, University of Maryland, College Park, MD 20742, USA. (yoonp@umd.edu)

ambient magnetic field, respectively. Since the term "maser" implies radiation, the instability involving *Z* mode may not be called a maser in a strict sense. However, *Z* mode may convert to *O* mode in the presence of density or magnetic field inhomogeneity, and because its excitation requires the relativistic correction to the cyclotron wave-particle resonance condition, the *Z*-mode instability qualifies as part of the general electron-cyclotron maser category.

[4] Spacecraft-borne receivers at both high and low altitudes in the Earth's auroral zone commonly detect *Z*-mode emissions, typically over a wide relative bandwidth. Extending from the *Z* cutoff up to $f_{ce} = \dfrac{\Omega}{2\pi}$ or $f_p = \dfrac{\omega_p}{2\pi}$, at high altitudes, and concentrated in the frequency range $f_p < f < f_{uh}$ at low altitudes, where $f_{uh} = \dfrac{\omega_{uh}}{2\pi}$ (see review by *LaBelle and Treumann* [2002, and references therein]). These modes often have transverse wavelengths. One possible source is refraction of beam-generated auroral Langmuir waves, but another possibility is direct excitation of the transverse waves through, for example, the maser instability. In the latter case, the most common and relevant source of free energy in the auroral zone is the loss cone in the electron distribution function.

[5] Direct excitation of *Z*-mode waves via loss cone cyclotron maser in the auroral ionosphere at altitudes of 300–600 km, followed by conversion to *O* mode, is the most widely accepted explanation for a class of radio emissions known as auroral roar observed at ground level [*Kellogg and Monson*, 1979; *Weatherwax et al.*, 1993; *Sato et al.*, 2012; *LaBelle*, 2012] and in space [*James et al.*, 1974; *Benson and Wong*, 1987]. These consist of emissions originating at locations in the bottomside and topside auroral ionosphere where f_{uh} matches a cyclotron harmonic. The first through fourth harmonics, corresponding to $f_{uh} = 2 - 5f_{ce}$, have been observed. The $2f_{ce}$ type is best documented; it is always left-hand polarized consistent with *O* mode and has been observed propagating downward and upward from the matching points in the auroral ionosphere. *Weatherwax et al.* [2002] show how observing multiple of these emissions can be used to remotely sense the density profile along auroral field lines. Recently, *Menietti et al.* [2012] report waves detected at Saturn that appear analogous to the $2f_{ce}$ roar observed at Earth. Substantial theoretical work supports the application of the loss cone driven *Z*-mode maser to these observations [e.g., *Yoon et al.*, 1996, 1998a, 2000, 2004]. However, the analysis to date has focused on maximum growth rates as a function of plasma-to-cyclotron-frequency ratio without regarding in detail how the growth rate varies as a function of the wave vector. A broader treatment is essential to understand the commonly observed cyclotron harmonic emissions. An outstanding problem is the mode conversion mechanism which could proceed by linear or nonlinear mechanisms. The linear mechanism has been favored in the literature [e.g., *Yoon et al.*, 1998b]; however, for any mechanism, in particular for linear mode conversion via the Ellis window, correctly calculating mode conversion efficiencies requires distinguishing between, for example, different wave number ranges of unstable *Z* modes, since the conversion efficiency can depend sensitively on the angle between the wave vector and the ambient magnetic field [*Yoon et al.*, 1998b]. Moreover, evaluating the

feasibility of a mode conversion mechanism requires an understanding of the *Z*-mode power near the ionospheric source, which is dependent on the wave growth as a function of wave vector.

[6] The importance of the ratio ω_p^2/Ω^2, not only for the *Z*-mode waves, but also for general cyclotron maser instability has been noted. *Hewitt et al.* [1982] and *Melrose et al.* [1984] were among the first to investigate the properties of normalized maximum growth rates for various magnetoionic modes as a function of ω_p/Ω. Of course, other physical input parameters such as the density ratio between the energetic loss cone electron and the background electrons, thermal energies associated with both the background and the loss cone, the loss cone angle, the smoothness associated with the loss cone boundary in the pitch angle space, all determine the maser instability characteristics. However, the above references as well as other literature since the 1980s generally elucidated that the most important parameter is ω_p^2/Ω^2. Similar works as those by *Hewitt et al.* [1982] and *Melrose et al.* [1984] were also carried out by *Sharma and Vlahos* [1984], *Winglee* [1985a, 1985b], *Winglee and Dulk* [1986], *Yoon et al.* [1996, 1998a], *Zhao and Wu* [2013], *Wu et al.* [2012], and *Zhao et al.* [2013]. However, a common feature in all these works is that the analyses were restricted to relatively low values of ω_p/Ω so that only the first two harmonic *X* and *O* modes (*X*1, *X*2, *O*1, and *O*2) and only *Z*1 mode were taken into account.

[7] For high ω_p/Ω it is well known that the growth of fast (*X* and *O*) modes are suppressed, but *Z* mode continues to grow. *Winglee and Dulk* [1986] first investigated this problem for ω_p/Ω ranging from ~ 4 to ~ 20, but they employed simplified growth rate expressions and adopted the Dory-Guest-Harris (DGH) electron distribution function, which does not faithfully represent the loss cone distribution. The DGH model was used in the literature because it facilitates mathematical manipulations, but strictly speaking, it only qualitatively represents the loss cone. Motivated by high-frequency electromagnetic waves observed at the quasi-perpendicular shock, *Yoon et al.* [2007] analyzed the high-harmonic maser instability that includes up to eighth harmonics of *X* and *O* modes and *Z* modes for a range of frequency ratio $0 < \omega_p/\Omega < 8$. However, in their analysis, they employed a simple cold ring beam electron distribution function. Finally, in order to explain the source of narrowband emission at Saturn, *Menietti et al.* [2010] analyzed the maser instability growth rate for *Z* modes up to the seventh harmonic over a range of frequency ratio that corresponds to $0 < \omega_p/\Omega < 7$.

[8] The present analysis is similar to that of *Menietti et al.* [2010] in that realistic loss cone model is employed for the growth rate calculation, and the maximum growth for *Z* mode, $\gamma_{\max}/\Omega$, is determined by carefully surveying the frequency and angular space (ω, θ) over which the growth occurs. However, the main difference is that, whereas *Menietti et al.* [2010] focused only on the gross maximum growth rate as a function of plasma-to-cyclotron frequency ratio ω_p/Ω, in the present paper, we carefully investigate the phenomenon of the *Z*-mode maser instability splitting into two separate branches, to wit, one with extremely narrow-banded characteristics and the other broad-banded in frequency. In the previous studies of the *Z*-mode maser instability, the distinction between the narrowband and

broadband emissions has not been made. Instead, for a given value of ω_p/Ω, the most unstable mode is simply determined, regardless of the detailed spectral characteristics.

[9] As it will turn out, the narrowband Z mode often has the higher temporal growth rate, so if one blindly determines the highest Z-mode growth rate, then one will more likely choose the narrowband mode. This band, however, turns out to have extremely short wavelengths, and is highly electrostatic. This implies that once the warm plasma effect is taken into account for the background electrons (in the present analysis, we resort to the cold-plasma approximation, i.e., magnetoionic theory), the mode may be damped by background thermal effects. Moreover, such a highly electrostatic mode may not likely convert to O mode easily. In contrast, the broadband Z mode, even though it often has a weaker growth rate, turns out to have a significant degree of electromagnetic (O mode) polarization, and is characterized by long wavelengths. These modes may easily convert to an escaping O mode radiation, and thus be observed by remote means. For the above mentioned reasons, it is useful to distinguish the broadband versus the narrowband Z modes when one discusses the most unstable mode characteristics. In the present paper, we thus carry out a detailed analysis of the Z-mode maser instability, by carefully distinguishing the two different branches.

[10] The organization of the paper is as follows: In section 2, we outline the basic theoretical formalism and present some sample dispersion relation and growth rate calculations. Section 3 is devoted to the discussion of the scaling behavior associated with the maximum growth rate, the emission angle, and the real frequency, as a function of the plasma-to-gyrofrequency ratios. Finally, the findings in the present paper is summarized in section 4.

2. Narrowband and Broadband Z-Mode Instabilities

[11] The essential details of the theoretical formalism are described in a companion paper [*Lee et al.*, 2013]. For the sake of completeness, we briefly outline the theoretical formalism, but we restrict ourselves to Z mode exclusively. The dispersion relation of interest to us is given by

$$N^2 = 1 - \frac{\omega_p^2}{\omega(\omega + \tau\Omega)},$$

$$\tau = \left(\sigma + \sqrt{\sigma^2 + \cos^2\theta}\right)\frac{\omega_p^2 - \omega^2}{|\omega_p^2 - \omega^2|},$$

$$\sigma = \frac{\omega\Omega\sin^2\theta}{2|\omega^2 - \omega_p^2|}, \qquad (1)$$

where $N^2 = c^2 k^2/\omega^2$ is the square of the index of refraction, k and ω being the wave number and angular frequency, respectively, and θ is the angle of propagation for the wave phase velocity. The Z mode is defined by its frequency range,

$$\omega_Z < \omega < \omega_Z^{\text{res}},$$

$$\omega_Z = \frac{1}{2}\left(\sqrt{\Omega^2 + 4\omega_p^2} - \Omega\right),$$

$$\omega_Z^{\text{res}} = \frac{1}{\sqrt{2}}\left[\omega_{uh}^2 + \sqrt{(\omega_p^2 - \Omega^2)^2 + 4\omega_p^2\Omega^2\sin^2\theta}\right]^{1/2}, \qquad (2)$$

where ω_Z is the Z-mode cutoff frequency and ω_Z^{res} is the Z-mode resonance frequency.

[12] Under the weakly relativistic approximation the temporal growth rate for Z mode can be shown to reduce to [*Lee et al.*, 2013]

$$\Gamma = \frac{\omega_p^2}{\omega}\frac{\pi^2}{R}\sum_{s=0}^{\infty}\left(\Theta(s\Omega - \omega)\int_{-1}^{1}d\mu Q_s(u_+, \mu)\right.$$

$$\left. + \Theta(\omega - s\Omega)\Theta(1 - \mu_s^2)\int_{\mu_s}^{1}d\mu\sum_{+,-}Q_s(u_\pm, \mu)\right),$$

$$u_\pm = N\mu\cos\theta \pm \sqrt{N^2\mu^2\cos^2\theta + 2\left(\frac{s\Omega}{\omega} - 1\right)},$$

$$\mu_s = \frac{\sqrt{2}}{N\cos\theta}\sqrt{1 - \frac{s\Omega}{\omega}},$$

$$Q_s(u, \mu) = \frac{\tau^2}{\tau^2 + \cos^2\theta}\frac{u^2(1 - \mu^2)}{|u - N\mu\cos\theta|}$$

$$\cdot\left[\frac{\omega}{\Omega}\left(K\sin\theta + \frac{\cos\theta}{\tau}(\cos\theta - Nu\mu)\right)\frac{J_s(b)}{b} + J_s'(b)\right]^2$$

$$\cdot\left(u\frac{\partial}{\partial u} + (Nu\cos\theta - \mu)\frac{\partial}{\partial\mu}\right)f(u, \mu),$$

$$\qquad (3)$$

where $u = p/mc$ is the normalized momentum, $\mu = p_{\parallel}/p$ represents the cosine of the pitch angle, and $b = (\omega/\Omega)Nu(1 - \mu^2)^{1/2}\sin\theta$ is the argument of the Bessel function. The quantities K and R are given by

$$K = \frac{\omega_p^2}{\omega_p^2 - \omega^2}\frac{\Omega\sin\theta}{\omega + \tau\Omega},$$

$$R = 1 + \frac{\omega_p^2(\tau^2\omega^2 - \omega_p^2\cos^2\theta)}{\omega^2(\omega + \tau\Omega)^2\sin^2\theta}\frac{\tau^2 - \cos^2\theta}{\tau^2 + \cos^2\theta}. \qquad (4)$$

[13] For the choice of electron distribution function $f(u, \mu)$, we consider a one-sided loss cone distribution function specified by

$$f(u, \mu) = \frac{1}{\pi^{3/2}\alpha^3 A}\exp\left(-\frac{u^2}{\alpha^2}\right)\left(1 - \tanh\frac{\mu - \mu_0}{\delta}\right),$$

$$A = 1 + \frac{\delta}{2}\left[\ln\left(\cosh\frac{1 + \mu_0}{\delta}\right) - \ln\left(\cosh\frac{1 - \mu_0}{\delta}\right)\right], \qquad (5)$$

where $\alpha = (2T_e/mc^2)^{1/2}$ represents the normalized thermal speed, T_e being the electron temperature defined in the unit of energy, μ_0 is the cosine of the loss cone angle, and δ is a parameter that defines the smoothness associated with the loss cone boundary. In addition to the energetic loss cone electrons, we also consider the background thermal electrons. In the stability analysis to follow, we consider that the ratio of number densities for the energetic-to-background electrons is 10%. The temperature for the cold electrons is assumed to $\sim 10^3$ Kelvin, corresponding to the normalized thermal speed $\alpha_0 = (2T_0/mc^2)^{1/2} = 5.8\times10^{-4}$. In what follows we consider a sample case of $\alpha = 0.1$ (corresponding to 2.56 keV thermal electron energy), $\mu_0 = 0.6$ (implying that the pitch angle corresponding to the loss cone is equal to 53.13°), the smoothness parameter $\delta = 0.25$, and a range of plasma-to-gyrofrequency ratio, ω_p/Ω.

[14] Figure 1 displays the two-dimensional phase space loss cone distribution function (in logarithmic colormap scale) versus $u_\perp = u(1 - \mu^2)^{1/2}$ and $u_{\parallel} = u\mu$. The curves
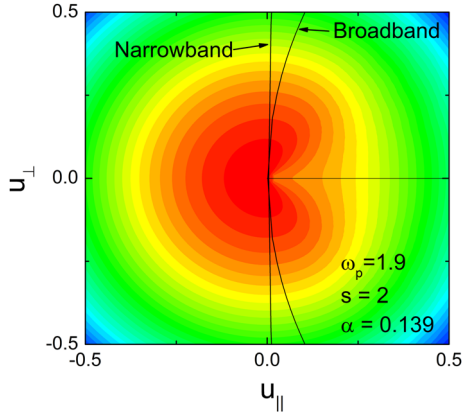
Figure 1. Colormap plot of $\log_{10} f(u, \mu)$ versus $u_\perp = u(1 - \mu^2)^{1/2}$ and $u_\parallel = u\mu$. Sample resonance circles corresponding to narrowband and broadband unstable Z modes are superposed on top of colormap plot of $f(u, \mu)$.

designated as "Narrowband" and "Broadband" have to do with the resonance circles, which we shall come back to near the end of the present paper. The parameters designated as $\omega_p = 1.9$, $s = 2$, and $\alpha = 0.139$ are related to the resonance circles, which again, we shall return to later. For the moment, it is sufficient to mention that the present loss cone distribution function features a one-sided loss cone for $u_\parallel > 0$.

[15] Figure 2 shows the Z-mode growth rate Γ/Ω versus ω/Ω and θ, for various values of ω_p/Ω, ranging from $\omega_p/\Omega = 1.732 \approx \sqrt{3}$, to 1.95. The first case of $\omega_p/\Omega = 1.732$ (Figure 2a) corresponds to the upper-hybrid matching condition $\omega_p^2/\Omega^2 = s^2 - 1$ with $s = 2$. In this case the unstable Z mode has an extremely narrow bandwidth, $\delta\omega/\Omega \sim \mathcal{O}(0.002)$, and the propagation angle is very close to 90°. As ω_p/Ω increases to 1.75 (Figure 2b), the bandwidth associated with the unstable mode noticeably increases, $\delta\omega/\Omega \sim \mathcal{O}(0.005)$, and the wave emission moves to smaller angles. The angular bandwidth also increases such that in the (ω, θ) space, the range of unstable Z mode takes on a crescent or semiarc shape.
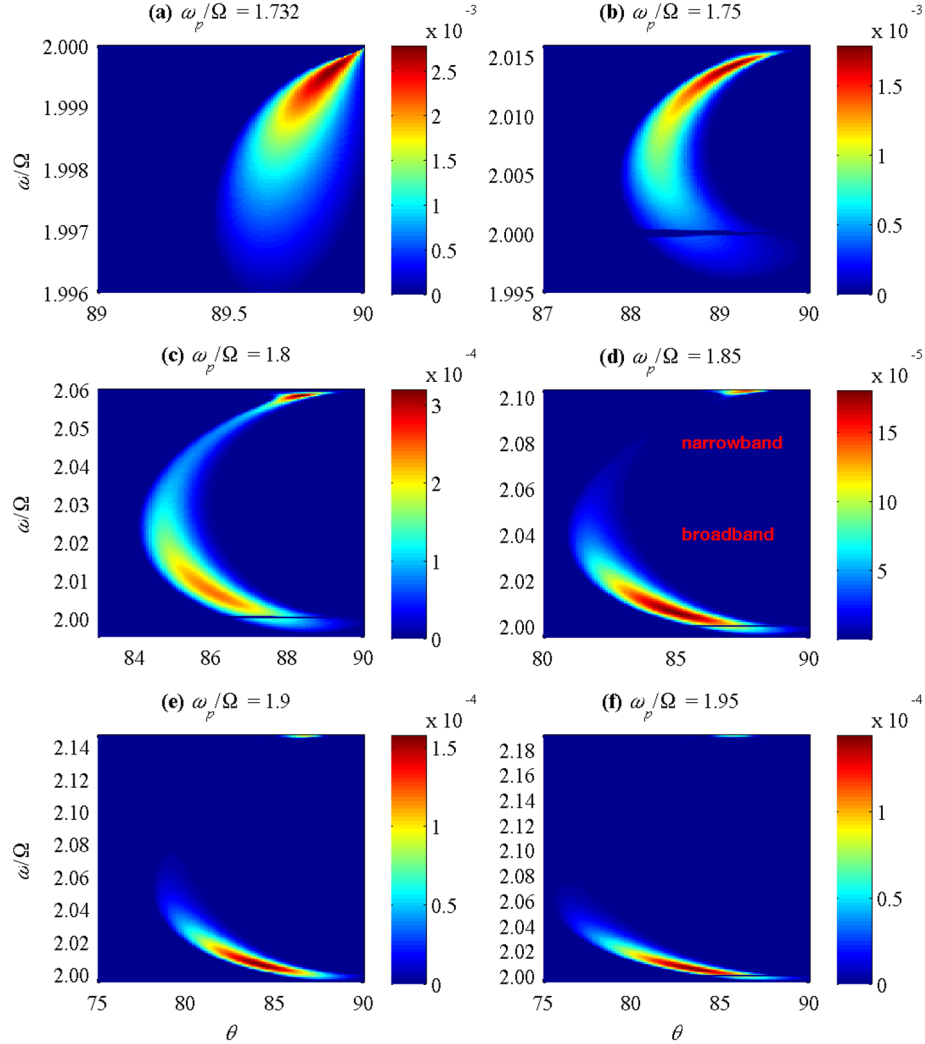

Figure 2. Z-mode growth rate γ/Ω versus ω/Ω and θ, in colormap format, for $\omega_p/\Omega =$ (a) 1.732, (b) 1.75, (c) 1.8, (d) 1.85, (e) 1.9, and (f) 1.95. Note how the near 90° Z mode for $\omega_p/\Omega = 1.732$ gradually split up into narrowband and broadband modes as ω_p/Ω increases.

(a) $\omega_p/\Omega = 1.732$

(b) $\omega_p/\Omega = 1.75$

(c) $\omega_p/\Omega = 1.8$

(d) $\omega_p/\Omega = 1.85$

narrowband

broadband

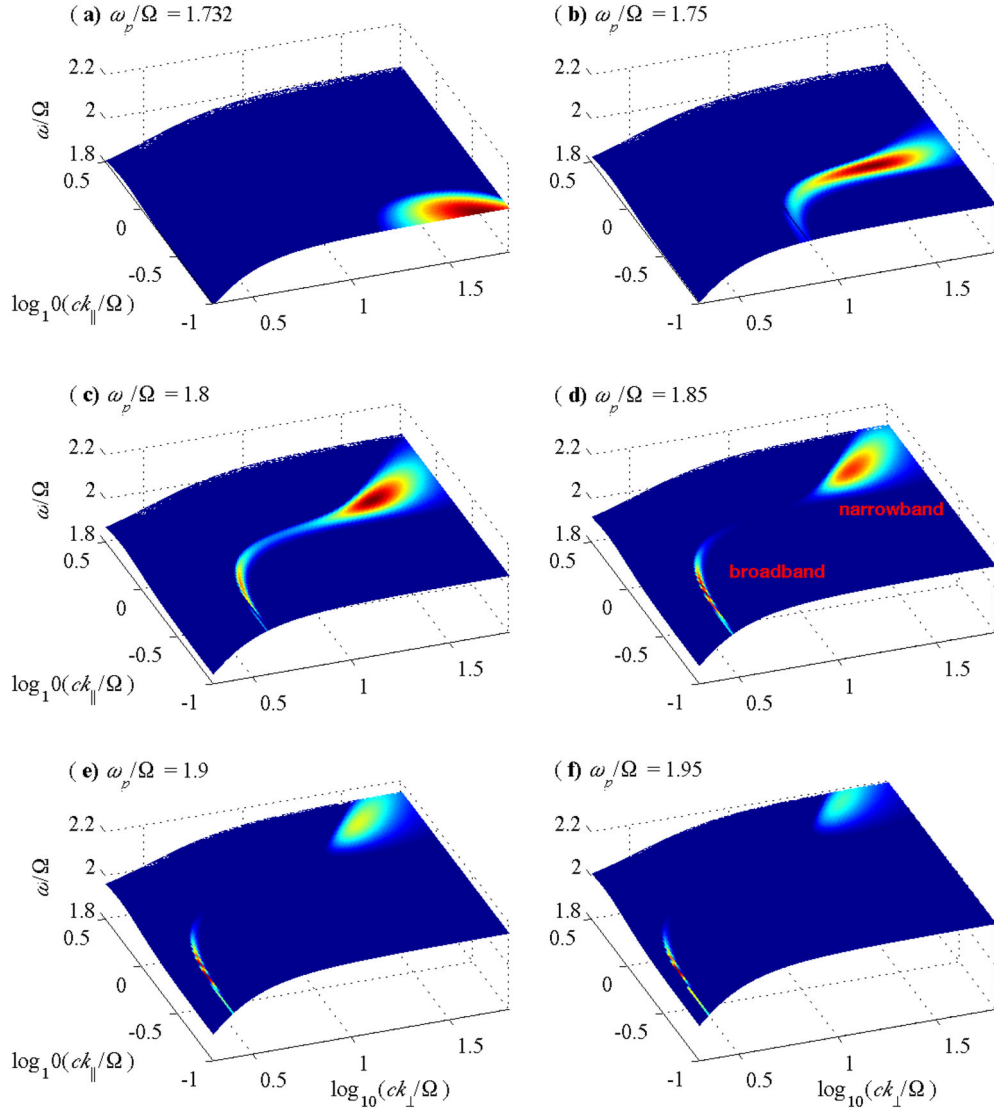**(e)** $\omega_p/\Omega = 1.9$

(f) $\omega_p/\Omega = 1.95$

Figure 3. The same as Figure 2 except that the results are plotted in dispersion surface format. The two horizontal axes are in logarithmic scale.

[16] For Figure 2c corresponding to $\omega_p/\Omega = 1.8$, the unstable Z mode now has two distinct peaks along the arc-shaped unstable region. The higher-frequency peak has an extremely narrow bandwidth, still on the order $\delta\omega/\Omega \sim \mathcal{O}(0.005)$, and also has higher growth rate. The lower frequency band has a significantly broader frequency range, $\delta\omega/\Omega \sim \mathcal{O}(0.02)$. Thus, starting with $\omega_p/\Omega = 1.8$, we begin to see that Z-mode instability splits into two distinct types and is operative over two separate frequency regimes, one is characterized by an extremely narrowband, while the second band has the property of appreciably broader frequency bandwidth. Moving on to Figure 2d where $\omega_p/\Omega = 1.85$, we observe that the separation between the two types of instabilities is complete, as we indicate so in the figure. The final two cases, Figures 2e and 2f corresponding to $\omega_p/\Omega = 1.9$ and 1.95, respectively, further show the separate branches of Z-mode instability, but as one can see, the narrowband branch gradually disappears as ω_p/Ω is increased. The dark horizontal lines that appears in some

figure panels correspond to the second-harmonic cyclotron damping by the background electrons.

[17] In Figure 3 we plot the same Z-mode growth rates in the dispersion surface format, namely, we superpose the growth rates in the colormap format over the real frequency ω/Ω plotted as a function of $ck_\perp/\Omega = ck\sin\theta/\Omega$ and $ck_\parallel/\Omega = ck\cos\theta/\Omega$. In this format, the real surface forms a manifold in the frequency, perpendicular and parallel wave number space, and the growth rate is indicated by the colormap. The wave numbers are plotted in logarithmic scale; thus, for instance, along $ck_\perp/\Omega$ axis, the numeric value 0 means $ck_\perp/\Omega = 1$, while 2 means $ck_\perp/\Omega = 100$.

[18] In this format, we again see that Figure 3a $\omega_p/\Omega = 1.732$ has the peak Z-mode growth occurring very close to 90° and that it has an extremely short perpendicular wavelengths. Such a regime corresponds to quasi-electrostatic polarization, and it is subject to thermal influence by background electrons. That is, once thermal effects associated with the background electron are taken into account, the real
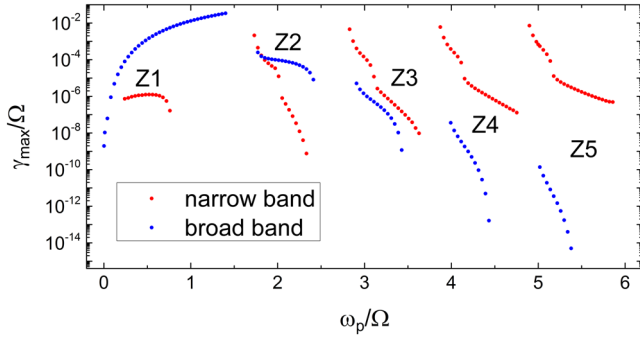
Figure 4. Local maximum growth rate γ_{max}/Ω corresponding to narrowband and broadband Z-mode instabilities versus ω_p/Ω.

frequency for such a short wavelength regime will be modified by the electron Bernstein mode effect, and the mode will also suffer cyclotron damping. In the present analysis, however, we do not consider such effects, since we treat the background electrons as cold as far as the real frequency is concerned (however, we do consider the damping effect by the background electrons).

[19] As ω_p/Ω increases to 1.75 (Figure 3b), the peak Z-mode growth moves toward small angles. When the result is plotted in (ω, θ) space, the result is Figure 2b. For Figure 3c where $\omega_p/\Omega = 1.8$, the Z-mode growth begins to split into two branches, each having local peaks. The clear separation between the two regimes can be seen in Figure 3d where $\omega_p/\Omega = 1.85$. The mode with a broader wave number range actually has a narrower frequency bandwidth, while the narrower strip of unstable mode in the wave number space is associated with the broader frequency bandwidth. This is because of the surface format representation of the dispersion relation. Because of the fact that the narrowband mode (indicated in the figure) occurs over a very flat region of the dispersion surface, the frequency bandwidth associated with this regime becomes extremely narrow. In contrast, even though the broadband Z mode appears as a narrow strip, since the dispersion surface along the strip has a gentle slope, this band appears as a broadband mode. However, when viewed in the present dispersion surface representation, the narrowband Z mode occupies a broad range of wave numbers, while the broadband Z mode appears as a narrow strip.

[20] Note that the flatness associated with the dispersion surface is related to the group velocity, whose magnitude $v_{group} = |\partial\omega/\partial\mathbf{k}|$ is related to the slope of the dispersion surface. Since the narrowband waves occur in a rather flat region of the dispersion surface, its spatial growth rate Γ/v_{group} will be significantly higher than that of the broadband mode.

[21] Figures 3e and 3f further illustrate the two separate Z modes, but as ω_p/Ω increases to 1.9 and to 1.95, it can be seen that the narrowband mode becomes weaker and weaker when compared with the broadband mode. This was already noted in Figure 2, although it is more clearly visible in Figure 3.

[22] As noted in section 1, previous studies of the Z-mode instability did not distinguish between the two different Z modes. It turns out that the narrowband mode usually

has higher growth rate. As a consequence, if one were to simply determine the maximum growth rate without discerning the spectral characteristics, one is more likely to pick the narrowband mode as the most relevant Z mode. However, as noted already, since the narrowband Z mode occurs for a short wavelength regime, this mode is subject to thermal modification by the background plasma effects. In contrast, the broadband Z mode is associated with relatively long wavelengths. As such, the mode is close to the O-mode dispersion surface, and it can easily convert to electromagnetic radiation with O-mode polarization in inhomogeneous plasmas through the so-called Ellis radio window. (The overall polarization characteristics was discussed in the companion paper by *Lee et al.* [2013].) Consequently, the broadband mode may escape the source region as the Z-mode maser. As a consequence, it is useful to separately treat the two types of Z modes. Here we note that the actual demonstration of Z- to O-mode conversion process is a complicated one that is beyond the scope of the present paper.

[23] In the present section, we have conducted the case study of Z-mode instability with wave frequency in the vicinity of 2Ω. The reason for this is because we have considered ω_p/Ω in the vicinity matching condition $\omega_p^2/\Omega^2 = s^2 - 1$ with $s = 2$. This situation can be termed, the Z2 mode maser, and it is highly relevant to the so-called $2f_{ce}$ auroral roar emission [*LaBelle et al.*, 1995; *Weatherwax et al.*, 1995; *Shepherd et al.*, 1997; *Hughes et al.*, 2001; *Samara et al.*, 2004]. For different values of ω_p/Ω, however, the Z mode instability may take place with frequency close to the fundamental electron gyrofrequency Ω in the case of lower value (in which case, it is Z1 maser), or higher harmonics, Z3, Z4, etc., for higher values of ω_p/Ω. Note that the auroral roar emission is detected up to fifth-harmonic electron cyclotron mode [*Sato et al.*, 2012; *LaBelle*, 2012]. In general, the frequency ratio ω_p/Ω must be sufficiently low for Z1 excitation to occur, while higher values of ω_p/Ω greater than 2 are expected to lead to high-harmonic Z modes, Z3, Z4, etc. In the next section, we shall repeat the similar calculation as in Figures 2 and 3 for other values of ω_p/Ω, but instead of displaying the detailed results as in Figures 2 and 3, we shall determine the local maxima corresponding to broadband and narrowband Z modes and plot the results as a function of ω_p/Ω.

[24] We shall also plot the propagation angle and frequency corresponding to local maxima versus ω_p/Ω. The information on the propagation angle corresponding to the maximum growth, θ_{max}, and the frequency corresponding to the maximum growth occurring at a given harmonic, with the harmonic mode number subtracted from the frequency, namely, $\omega_{max} - s\Omega$, are useful in order to completely characterize the harmonic Z mode instability driven by the loss cone electron distribution.

3. Property of Narrowband and Broadband Z-Mode Instabilities Near Maximum Growths

[25] Figure 4 displays the local growth rate peaks associated with the narrowband and broadband Z-mode instabilities versus ω_p/Ω. As Figures 2 and 3 already showed, the narrowband and broadband Z modes appear to merge into a single unstable mode when ω_p/Ω approaches $\sqrt{3}$,

which is the lowest possible upper-hybrid matching condition, $\omega_p^2/\Omega^2 = s^2 - 1$ with $s = 2$. However, as already seen in Figures 2 and 3, as ω_p/Ω increases, the two branches split up. It is interesting to note that the broadband *Z* mode generally has higher growth rate for ω_p/Ω greater than 1.732. This is consistent with Figures 2 and 3.

[26] In the case of *Z*3, again, the two unstable modes begin to appear when $\omega_p/\Omega = \sqrt{8}$, which is the next exact upper-hybrid matching condition, $\omega_p^2/\Omega^2 = s^2 - 1$ with $s = 3$. In this case, however, as ω_p/Ω becomes higher than $\omega_p/\Omega = \sqrt{8}$, the narrowband *Z*3 retains the higher maximum growth rate. The similar tendency can be seen for higher harmonic *Z* modes.

[27] For low values of ω_p/Ω, on the other hand, the upper-hybrid matching condition becomes irrelevant since $\omega_p^2/\Omega^2 = s^2 - 1$ has no solutions for $s < 2$. Nevertheless, *Z*1-mode instability is excited by the maser mechanism. For *Z*1 instability, however, the broadband mode generally dominates over the narrowband branch.

[28] The maximum growth rate plot versus ω_p/Ω provides a useful guide to the condition for *Z*-mode maser excitation. However, in order to complete the analysis, it is useful to consider the wave propagation angle at which the local maximum growths occur, i.e., θ_{max}, as a function of ω_p/Ω as well. As can be seen from Figures 2 and 3, the narrow- and broadband *Z* modes have wave propagation angles that are generally oblique, but they can vary substantially. Figure 5 thus displays the propagation angle corresponding to the local maxima for narrowband and broadband *Z* modes, θ_{max}, versus ω_p/Ω. Recall that the terms broadband and narrowband refer to the frequency bandwidth characterizing the positive growth for a particular ratio of ω_p/Ω, not to the range over which the frequency of maximum growth varies. The broadband *Z* mode can have a substantial field-aligned wave vector component, as can be discerned from Figure 5. As noted, this type of *Z* mode can be of importance, even though it is associated with generally weaker growth rate, as they can escape the source region via mode conversion.

[29] The frequencies for *Z*-mode masers are very close to the harmonics of electron gyrofrequency in general, and so they can be characterized by the designations, *Z*1, *Z*2, etc. Nevertheless, the frequencies at which the local peaks occur for narrowband and broadband *Z* modes varies considerably, especially for the narrowband mode. Shown in Figure 6 is the plot of harmonic mode number-subtracted frequency corresponding to the peak growths, $(\omega_{max} - s\Omega)/\Omega$,
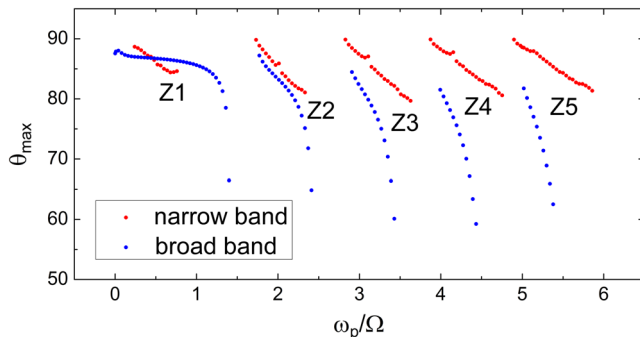

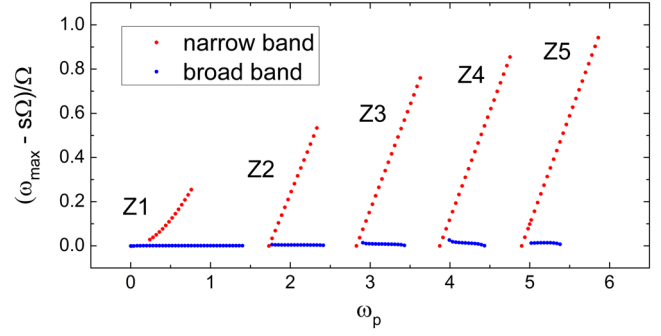**Figure 6.** The wave frequency corresponding to narrowband and broadband *Z*-mode instabilities, $(\omega_{max} - n\Omega)/\Omega$, versus ω_p/Ω.

for $s = 1, 2, \ldots, 5$, versus ω_p/Ω. It can be seen that the broadband *Z* modes are excited close to each harmonic, but the narrowband mode steadily increases between each harmonic. This is because the narrowband *Z* modes are essentially quasi-electrostatic upper-hybrid waves such that their frequencies are linearly proportional to ω_p, especially for high values of ω_p/Ω. As a consequence, when the ratio ω_p/Ω increases, the corresponding wave frequency for unstable narrowband *Z* mode simply follows the ratio ω_p/Ω and monotonically increases as ω_p/Ω increases.

[30] Finally, we illustrate the difference between the narrowband and broadband *Z* mode from another perspective, which is from the viewpoint of wave-particle resonance condition. The basic mechanism for the weakly relativistic *Z*-mode maser instability is the relativistic cyclotron resonance between the electrons and these waves. In the weakly relativistic approximation the resonance condition $\omega - s\Omega/\gamma - k_\parallel v_\parallel = 0$ can be expressed as

$$u_\perp^2 + (u_\parallel - u_0)^2 = r^2,$$
$$u_0 = N\cos\theta,$$
$$r^2 = N^2\cos^2\theta + \frac{2(s\Omega - \omega)}{\omega}. \qquad (6)$$

If we consider the case of $\omega_p/\Omega = 1.9$, normalized thermal energy $\alpha = 0.139$, and $s = 2$, and consider the frequencies and angles for the narrow versus broadband *Z* modes corresponding to $(\omega, \theta) \sim (2.145879\Omega, 86.834170°)$ and $(\omega, \theta) \sim (2.004472\Omega, 84.582914°)$, respectively, at which the highest growth occurs, we obtain the resonance circles depicted in Figure 1. We superpose the resonance circles on top of the colormap plot of the model loss cone distribution function $\log_{10} f(u, \mu)$. The result is Figure 1. It is interesting to note that the resonance circles associated with both types of *Z* modes have very large radii such that over the velocity space for which the electron distribution function has positive gradients, $\partial f/\partial u_\perp > 0$, the resonance conditions practically reduce to semistraight lines. This is particularly true with the narrowband *Z* mode.

4. Summary

[31] In the present paper we have revisited the problem of *Z*-mode maser instability by focusing on the difference between the broadband versus narrowband frequency structure associated with the unstable upper-hybrid/*Z* mode

Figure 5. The wave propagation angle corresponding to narrowband and broadband *Z*-mode instabilities, θ_{max}, versus ω_p/Ω.

driven by the electron loss cone distribution. Here we extend the notion of the maser to the *Z* mode even though it is not the fast electromagnetic radiation. However, since the *Z* mode can escape the source region in an inhomogeneous plasma by a mode conversion and be detected as radiation, such as in the case of auroral roar emission [*LaBelle et al.*, 1995; *Weatherwax et al.*, 1995; *Yoon et al.*, 1996, 1998b; *Shepherd et al.*, 1997; *Hughes et al.*, 2001; *Samara et al.*, 2004; *Sato et al.*, 2010, 2012; *LaBelle*, 2012], we include it in the general maser instability category.

[32] We find that the *Z* mode growth is generally enhanced when the ratio of plasma-to-gyrofrequency, ω_p/Ω, satisfies the so-called "upper-hybrid matching" condition, $\omega_p^2/\Omega^2 = s^2 - 1$, where $s = 1, 2, 3, \ldots$, which is a well-known characteristics. However, the new finding has to do with the *Z*-mode characteristics when ω_p/Ω begins to deviate from the exact matching condition. We found that as ω_p/Ω begins to increase from the value that satisfies the exact matching at any given *s* value, the *Z*-mode growth rate begins to split into two parts, one with an extremely narrow frequency bandwidth over which the positive growth occurs, while the second band, usually associated with the weaker growth rate, has a broadband property.

[33] As the broadband *Z* mode has long wavelengths with significant *O*-mode polarization, we believe that this mode may be important for remote observation, as it can easily convert to electromagnetic *O*-mode radiation. Moreover, the narrowband *Z* mode is highly susceptible to the background electron thermal effects since it is characterized by extremely short wavelengths. For this reason, the broadband *Z* mode may be of more practical importance than the narrowband mode. In the past, however, the distinction between the narrowband and broadband *Z* mode were not made, and as such when considering the maximum temporal or spatial growth rate for the *Z* mode, for instance, the mode with the highest growth rate was simply chosen [*Winglee and Dulk*, 1986; *Menietti et al.*, 2010]. This procedure might have preferentially picked the narrowband mode over the broadband branch.

[34] In order to clearly distinguish the two types of *Z* mode we have thus regenerated the maximum growth rate versus ω_p/Ω plot for both narrowband and broadband modes, and we have also plotted the wave propagation angle corresponding to the maximum growths and the wave frequency at which the maximum growth occurs.

[35] The importance and application of the present paper may be associated with the auroral radio emission from the ionospheric source at altitudes of 300–600 km, which is believed to be *Z*-mode waves excited via loss cone cyclotron maser instability, followed by conversion to *O* mode. These are known as auroral roar observed at ground level. Another immediate application may be that of in situ radio waves at Saturn that appear analogous to the auroral roar observed at Earth. Analysis of *Z*-mode excitation to date has focused mainly on maximum growth rates as a function of ω_p/Ω without regarding in detail how the growth rate varies as a function of the wave vector. Assuming that the excited *Z*-mode waves linearly convert to *O* mode and be detected on the ground (in the case of auroral roar), it is essential to correctly distinguish different wave number ranges of unstable *Z* modes, since the conversion efficiency can depend sensitively on the angle between the wave vector

and the ambient magnetic field. In this regard, the present analysis can be useful for such a mode conversion study, even though the demonstration of *Z*- to *O*-mode conversion process is beyond the scope of the present paper.

References

Benson, R. F., and H. K. Wong (1987), Low-altitude ISIS 1 observations of auroral radio emissions and their significance to the cyclotron maser instability, *J. Geophys. Res.*, *92*, 1218–1230.

Begelman, M. C., R. E. Ergun, and M. J. Rees (2005), Cyclotron maser emission from Blazar jets?, *Astrophys. J.*, *625*, 51–59.

Bingham, R., B. J. Kellett, R. A. Cairns, J. Tonge, and J. T. Mendonça (2003), Cyclotron maser radiation from astrophysical shocks, *Astrophys. J.*, *595*, 279–284.

Farrell, W. M., M. D. Desch, and P. Zarka (1999), On the possibility of coherent cyclotron emission from extrasolar planets, *J. Geophys. Res.*, *104*, 14,025–14,032.

Gurnett, D. A., et al. (2004), The Cassini radio and plasma wave investigation, *Space Sci. Rev.*, *114*, 395–463.

Hallinan, G., et al. (2007), Periodic bursts of coherent radio emission from an ultracool dwarf, *Astrophys. J.*, *663*, L25.

Hallinan, G., A. Antonova, J. G. Doyle, S. Bourke, C. Lane, and A. Golden (2008), Confirmation of the electron cyclotron maser instability as the dominant source of radio emission from very low mass stars and brown dwarfs, *Astrophys. J.*, *684*, 644–653.

Hess, S., F. Mottez, and P. Zarka (2007), Jovian *S* burst generation by Alfvén waves, *J. Geophys. Res.*, *112*, A11212, doi:10.1029/2006JA012191.

Hewitt, R. G., D. B. Melrose, and K. G. Rönnmark (1982), The loss-cone driven electron-cyclotron maser, *Aust. J. Phys.*, *35*, 447–471.

Hughes, J. M., J. LaBelle, and J. Watermann (2001), Statistical and case studies of $2f_{ce}$ auroral roar observed with a medium frequency interferometer, *J. Geophys. Res.*, *106*, 21,147–21,156.

James, H. G., E. L. Hagg, and L. P. Strange (1974), Narrowband radio noise in the topside ionosphere, *AGARD Conf. Proc.*, *AGARD-CP-138*, 241247.

Kellogg, P. J., and S. J. Monson (1979), Radio emissions from the aurora, *Geophys. Res. Lett.*, *6*, 297–300.

LaBelle, J. (2012), First observations of $5f_{ce}$ auroral roars, *Geophys. Res. Lett.*, *39*, L19106, doi:10.1029/2012GL053551.

LaBelle, J., M. L. Trimpi, R. Brittain, and A. T. Weatherwax (1995), Fine structure of auroral roar emissions, *J. Geophys. Res.*, *100*, 21,953–21,960.

LaBelle, J., and R. A. Treumann (2002), Auroral radio emissions, 1. Hisses, roars, and bursts, *Space Sci. Rev.*, *101*, 295–440.

Lee, L. C., and C. S. Wu (1980), Amplification of radiation near cyclotron frequency due to electron population inversion, *Phys. Fluids*, *23*, 1348.

Lee, S.-Y., S. Yi, D. Lim, H.-E. Kim, J. Seough, and P. H. Yoon (2013), Loss-cone driven cyclotron maser instability, *J. Geophys. Res. Space Physics*, *118*, doi:10.1002/2013JA019298.

Melrose, D. B., R. G. Hewitt, and G. A. Dulk (1984), Electron-cyclotron maser emission: Relative growth and damping rates for different modes and harmonics, *J. Geophys. Res.*, *89*, 897–904.

Menietti, J. D., P. H. Yoon, S.-Y. Ye, B. Cecconi, and A. M. Rymer (2010), Source mechanism of Saturn narrowband emission, *Ann. Geophys.*, *28*, 1013–1021.

Menietti, J. D., Y. Y. Shprits, R. B. Horne, E. E. Woodfield, G. B. Hospodarsky, and D. A. Gurnett (2012), Chorus, ECH, and Z mode emissions observed at Jupiter and Saturn and possible electron acceleration, *J. Geophys. Res.*, *117*, A12214, doi:10.1029/2012JA018187.

Nichols, J. D., M. R. Burleigh, S. L. Casewell, S. W. H. Cowley, G. A. Wynn, J. T. Clarke, and A. A. West (2012), Origin of electron cyclotron maser induced radio emissions at ultracool dwarfs: Magnetosphere-ionosphere coupling currents, *Astrophys. J.*, *760*, 59.

Pritchett, P. L. (1984), Relativistic dispersion, the cyclotron maser instability, and auroral kilometric radiation, *J. Geophys. Res.*, *89*, 8957–8970.

Pritchett, P. L., and R. J. Strangeway (1985), A simulation study of kilometric radiation generation along an auroral field line, *J. Geophys. Res.*, *90*, 9650–9662.

Pritchett, P. L. (1986), Cyclotron maser radiation from a source structure localized perpendicular to the ambient magnetic field, *J. Geophys. Res.*, *91*, 13,569–13,581.

Pritchett, P. L., R. J. Strangeway, C. W. Carlson, R. E. Ergun, J. P. McFadden, and G. T. Delory (1999), Free energy sources and frequency bandwidth for the auroral kilometric radiation, *J. Geophys. Res.*, *104*, 10,317–10,326.

Pritchett, P. L., and R. M. Winglee (1989), Generation and propagation of kilometric radiation in the auroral plasma cavity, *J. Geophys. Res.*, *94*, 129–143.

Speirs, R. K. D. C., et al. (2011), Auroral magnetospheric cyclotron emission processes: Numerical and experimental simulations, *Plasma Phys. Control. Fusion*, *53*, 074015, doi:10.1088/0741-3335/53/7/074015.

Samara, M., J. LaBelle, C. A. Kletzing, and S. R. Bounds (2004), Rocket observations of structured upper hybrid waves at $f_{uh} = 2f_{ce}$, *Geophys. Res. Lett.*, *31*, L22804, doi:10.1029/2004GL021043.

Sato, Y., T. Ono, N. Sato, and R. Fujii (2010), MF/HF auroral radio emissions emanating from the topside ionosphere, *Geophys. Res. Lett.*, *37*, L14102, doi:10.1029/2010GL043731.

Sato, Y., T. Ono, N. Sato, and Y. Ogawa (2012), First observations of $4f_{ce}$ auroral roar emissions, *Geophys. Res. Lett.*, *39*, L07101, doi:10.1029/2012GL051205.

Sharma, R. R., and L. Vlahos (1984), Comparative study of the loss cone-driven instabilities in the low solar corona, *Astrophys. J.*, *280*, 405–415.

Shepherd, S. G., J. LaBelle, and M. L. Trimpi (1997), The polarization of auroral radio emissions, *Geophys. Res. Lett.*, *24*, 3161–3164.

Tang, J. F., and D. J. Wu (2009), Electron-cyclotron maser emission by power-law electrons in coronal loops, *A & A*, *493*, 623–628.

Treumann, R. A. (2006), The electron cyclotron maser for astrophysical application, *Astron. Astrophys. Rev.*, *13*, 229–315, doi:10.1007/s00159-006-0001-y.

Trigilio, C., P. Leto, G. Umana, C. S. Buemi, and F. Leone (2011), Auroral radio emission from stars: The case of CU Virginis, *Astrophys. J.*, *739*, L10.

Weatherwax, A. T., J. LaBelle, M. L. Trimpi, and R. Brittain (1993), Ground-based observations of radio emissions near $f_{ce|}$ and $3f_{ce}$ in the auroral zone, *Geophys. Res. Lett.*, *20*, 1447, doi:10.1029/GL020i014p01447.

Weatherwax, A. T., J. LaBelle, M. L. Trimpi, A. Treumann, J. Minow, and C. Deehr (1995), Statistical and case studies of radio emissions observed near $2f_{ce}$ and $3f_{ce}$ in the auroral zone, *J. Geophys. Res.*, *100*, 7745–7757.

Weatherwax, A. T., P. H. Yoon, and J. LaBelle (2002), Interpreting observations of MF/HF radio emissions: Unstable wave modes and possibilities to passively diagnose ionospheric densities, *J. Geophys. Res.*, *107*(A8), 1213, doi:10.1029/2001JA000315.

Willes, A. J., and K. Wu (2004), Electron-cyclotron maser emission from white dwarf pairs and white dwarf planetary systems, *Mon. Not. R. Astron. Soc.*, *348*, 285–296.

Winglee, R. M. (1985a), Effects of a finite plasma temperature on electron-cyclotron maser emission, *Astrophys. J.*, *291*, 160–169.

Winglee, R. M. (1985b), Fundamental and harmonic electron cyclotron maser emission, *J. Geophys. Res.*, *90*, 9663–9674.

Winglee, R. M., and G. A. Dulk (1986), The electron-cyclotron maser instability as a source of plasma radiation, *Astrophys. J.*, *307*, 808–819.

Winglee, R. M., and P. L. Pritchett (1986), The generation of low-frequency electrostatic waves in association with auroral kilometric radiation, *J. Geophys. Res.*, *91*, 13,531–13,541.

Wu, C. S., and L. C. Lee (1979), A theory of the terrestrial kilometric radiation, *Astrophys. J.*, *230*, 621–626.

Wu, C. S., C. B. Wang, D. J. Wu, and K. H. Lee (2012), Resonant wave-particle interactions modified by intrinsic Alfvénic turbulence, *Phys. Plasmas*, *19*, 082902, doi:10.1063/1.4742989.

Yoon, P. H., A. T. Weatherwax, and T. J. Rosenberg (1996), Lower ionospheric cyclotron maser theory: A possible source of $2f_{ce}$ and $3f_{ce}$ auroral radio emissions, *J. Geophys. Res.*, *101*, 27,015–27,026.

Yoon, P. H., A. T. Weatherwax, and T. J. Rosenberg (1998a), On the generation of auroral radio emissions at harmonics of the lower ionospheric electron cyclotron frequency: *X*, *O*, and *Z* mode maser calculations, *J. Geophys. Res.*, *103*, 4071–4078.

Yoon, P. H., A. T. Weatherwax, T. J. Rosenberg, J. LaBelle, and S. G. Shepherd (1998b), Propagation of medium frequency (1–4 MHz) auroral radio waves to the ground via the *Z*-mode radio window, *J. Geophys. Res.*, *103*, 29,267–29,275.

Yoon, P. H., A. T. Weatherwax, and J. LaBelle (2000), Discrete electrostatic eigenmodes associated with ionospheric density structure: Generation of auroral roar fine frequency structure, *J. Geophys. Res.*, *105*, 27,589–27,596.

Yoon, P. H., C. B. Wang, and C. S. Wu (2007), Ring-beam driven maser instability for quasi-perpendicular shocks, *Phys. Plasmas*, *14*(022901), doi:10.1063/1.2437118.

Zarka, P. (1998), Auroral radio emissions at the outer planets: Observations and theories, *J. Geophys. Res.*, *103*, 20,159–20,194.

Zhao, G. Q., and C. S. Wu (2013), Emission of radiation induced by pervading Alfvén waves, *Phys. Plasmas*, *20*(034503), doi:10.1063/1.4798493.

Zhao, G. Q., L. Chen, Y. H. Yan, and D. J. Wu (2013), Effects of Alfvén waves on electron cyclotron maser emission in coronal loops and solar type I radio storms, *Astrophys. J.*, *770*, 75.